Carbon 203 (2023) 620–629

Contents lists available at ScienceDirect

Carbon

journal homepage: www.elsevier.com/locate/carbon

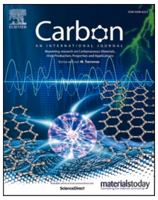

Ultra-high thermal sensitivity of graphene microfiber

Huan Lin [a,b,1], Nicholas Hunter [b,1], Hamidreza Zobeiri [b], Yanan Yue [c,**], Xinwei Wang [b,*]

[a] School of Environmental and Municipal Engineering, Qingdao University of Technology, Qingdao, Shandong, 266033, PR China
[b] Department of Mechanical Engineering, Iowa State University, Ames, IA, 50011, USA
[c] School of Power and Mechanical Engineering, Wuhan University, Wuhan, Hubei, 430072, PR China

ARTICLE INFO

Keywords:
Graphene microfiber
Ultra thermal sensitivity
Thermal conductivity
Cryogenic temperature
Electrical resistance

ABSTRACT

Graphene-based micro/nanoscale materials have not been used much for thermal sensing while they have great potential advantages over current sensors for micro/nanoscale measurement. This work reports on the discovery of ultra thermal sensing capability, especially at cryogenic temperatures for graphene microfibers (GMFs). From 295 K down to 11 K, the electrical resistance of GMF increases by around five orders of magnitude (10^5-fold). GMF's extreme thermal sensitivity is explored by using it for dynamically measuring its thermophysical properties. At 25 K, a temperature change as small as 0.027 K can be sensed with high confidence. Moreover, the fibers still have extreme sensitivity after current annealing. When the annealing temperature becomes higher, the microstructure of the material improves considerably, thereby ensuring application robustness in thermally hostile environment. GMF presents a novel ultra-sensitive material for temperature measurement at the micro/nanoscale, especially at cryogenic temperatures while its temporal response can reach a level of ms.

1. Introduction

Temperature is a fundamental physical parameter and its sensing is critical in many areas, including energy conversion, thermal design, material synthesis, and integrated electrical circuits. Thermocouples, resistance temperature detectors (RTDs) and thermistors are commonly used for temperature measurement in domestic, industrial, and medical applications. The choice of a particular sensor depends on the required accuracy, response speed, temperature range, thermal coupling, cost, and so on [1]. Thermocouples are one of the most popular and economical temperature sensors. The fundamental principle of thermocouple is the thermoelectric effect or Seebeck effect [2]. Due to the thermoelectric effect, a thermocouple produces a temperature-dependent voltage which can be interpreted as a measurement of temperature. Thermocouples are capable of monitoring temperatures between −270 and 3000 °C [3]. Their main drawbacks are their low sensitivity (microvolts per degree) and lower accuracy than thermistors and the need for a reference temperature [1].

Radiation thermometry is a non-contact technique for measuring surface temperatures over a wide range of temperatures. Based on Planck's law, the radiance depends on surface temperature and emissivity of the object. However, the emissivity of a hot object is often unknown and varies with the surface morphology, composition and phase of the object, and also varies with wavelength and temperature [4]. Therefore, in many practical cases, the "true" temperature cannot be accurately determined, and this is the main difficulty encountered in radiometric temperature measurement. Temperature measurements by radiation thermometry may also be affected by background radiation reflected at the sample surface into the signal detection system, leading to errors in temperature measurements [5–7]. A thermistor is a temperature-sensitive resistor made of a semiconductor metal oxide (such as oxide of manganese, cobalt, nickel, copper, iron or titanium) [8]. The disadvantage of thermistors is that they are susceptible to misalignment and drift due to changes in the semiconductor material [3]. Among several temperature sensors, ceramic-based thermistors have advantages in terms of manufacturing cost, sensitivity and response speed [1].

Monolayer graphene is composed of two-dimensional (2D) honeycomb structure consisting of sp^2 hybridized carbon atoms [9,10]. Over more than a decade, graphene has attracted a great deal of attention for its numerous fascinating properties, including strong mechanical strength [11], giant electron mobility [12,13] and excellent thermal

---

* Corresponding author.
** Corresponding author.
E-mail addresses: yyue@whu.edu.cn (Y. Yue), xwang3@iastate.edu (X. Wang).
[1] Authors contributed equally.

https://doi.org/10.1016/j.carbon.2022.12.013
Received 20 July 2022; Received in revised form 3 December 2022; Accepted 5 December 2022

conductivity [14,15]. These unique properties make it an advantageous material for use as nanoscale sensors [16], especially for heat flow and temperature sensing applications [17,18]. Li et al. found the reduced graphene oxide foam (RGOF) shows temperature sensitivity based upon thermoelectric effects in the graphene. The RGOF is capable of sensing heat and cold and measuring the heated/cooled areas under zero operating voltage [19]. Graphene has a higher temperature coefficient of resistance (TCR) than platinum, resulting in low thermal inertia and high sensitivity to temperature changes. The TCR is temperature dependent. At RT, the TCR is determined as $\sim -0.007\ C^{-1}$ for a bi-layer graphene. For monolayer graphene, its TCR is strongly affected by structural defects and substrate (for supported graphene). Values in the range of -0.00147 to $-0.003\ C^{-1}$ have been reported [20–22]. The TCR of graphene oxide is very large and it decreases gently between 200 and 350 K in the region of -0.024 to $-0.04\ C^{-1}$ [23]. Lee et al. found the TCR of graphene electrode is $-0.0148\ K^{-1}$ at 298 K, which is about 3 orders of magnitude higher than that of carbon nanotubes [24].

In this work, we synthesize graphene microfibers (GMF) by one-step dimensionally confined hydrothermal method. From thermal transport characterization we discover that the electrical resistance of GMF is extremely sensitive to temperature change, especially at low temperatures/cryogenic states. Such extreme sensing capability is fully investigated in thermal transport properties measurement. Finally, by the way of current annealing, the properties of structure and resistance variation are evaluated for their robustness in thermally hostile environment. GMF fibers are demonstrated to be a promising ultra-sensitive temperature sensor.

2. Material preparation and structure

The GMF is fabricated by one-step dimensionally confined hydrothermal method [25]. First, we use a syringe to inject 8 mg/ml aqueous graphene oxide suspension into two kinds of glass pipelines of inner diameters of 0.4 mm and 1.1 mm. The graphene oxide suspension is purchased from Changzhou Carbonvex Nano Technology Co. Before using, it was ultrasonically dispersed for 2 h. The two ends of pipelines are sealed with spirit lamp and then baked in an oven at 230 °C for 2 h as shown in Fig. 1(a). Baking is essential for the preparation process as the graphene oxide is liquid before baking. The time and temperature of baking influences the structure of GMF, but they are not the focus of this manuscript. In future, we will prepare materials under different baking conditions to study it specifically. Impurities and functional groups are very important to the ultra-sensing capability of the GMFs. However, it is difficult to identify the impurities and functional groups in them, as the composition of the solution is indeterminate. However, we can control the concentration and composition of the solution and the baking process to control the impurities and functional groups. These will influence the sensitivity of sensor. But each sensor can be calibrated in advance, and they will not be exactly the same. All the chemical reaction takes place in the glass pipe and is constrained within the micro

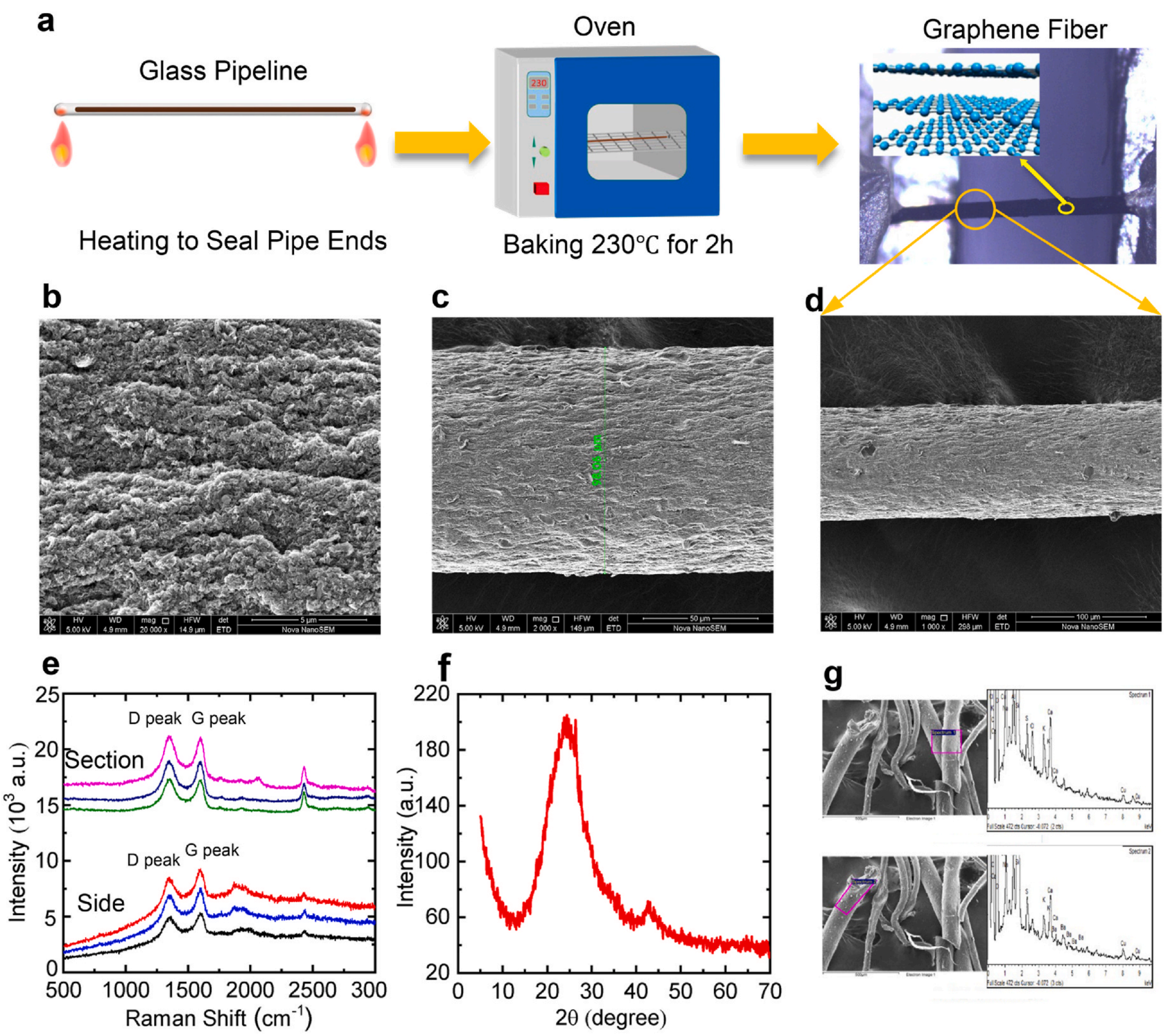

Fig. 1. (a) Schematic of GMF synthesis procedures. (b)–(d) SEM images showing morphology and structure of the GMF. (e) Raman spectrum of the GMF sample from section and side. (f) XRD diffractogram. (g) EDX spectra of the GMF. (A colour version of this figure can be viewed online.)

dimension provided by the glass pipe. Finally, GMFs matching the pipeline's geometry are synthesized. The preformed GMFs are released from the broken pipeline and dried in air. The dried GMFs almost maintain their original lengths, but their diameters are reduced to ~38 μm and ~93 μm because of water loss. The diameter and length of the fiber can be controlled by simply using a glass pipe with a pre-designed length and inner diameter. GMF has excellent performances and characteristics, such as good strength, low weight, high flexibility, ease of functionalization, controllable shaping and stitchability.

The morphological and structural characteristics of the GMFs are studied by using Scanning Electron Microscopy (SEM), Raman Spectroscopy, x-ray diffraction (XRD) and Energy Dispersive X-Ray Spectroscopy (EDX). As it is indicated in the SEM images in Fig. 1(b)–(d), the surface of the GMF is not completely uniform, and there are small ridges on it. Fig. 1(e) shows the Raman spectra of the GMF sample from section and side. The D peak indicates the strong defect level in the sample. The D and G peaks overlap and are not sharp, demonstrating various functional groups making the sample have some graphene oxide-like structure. The presence of impurities and oxygen-containing functional groups will cause additional scattering of electrons and affect the electrical resistance.

The XRD pattern of GMF is determined by a Bruker D8-Focus Bragg-Brentano X-ray Powder Diffractometer with a Cu radiation source (λ = 1.5418 Å). Fig. 1(f) is the XRD pattern of GMF from 0 to 70° of 2θ. The interlayer spacing of GMF calculated using the Scherrer formula is 0.8 nm, which is much bigger than 0.33553 nm reported for single-crystal graphite [26], confirming the existence of functional groups and impurities in GMF. Fig. 1 (g) is the EDX result. It shows there are Na, Al, Si, Ca, and other kinds of elements in GMF and verifies the above conclusion further.

3. High thermal probing sensitivity of GMF

The resistance measurement of samples is obtained by passing a small current (1.2 nA-152 μA) through it and measuring the voltage drop across it. The sample is suspended on two electrodes, and its ends are closely connected to the electrodes through silver paste. The average diameter and the length of sample 1 is 37.9 μm and 983 μm. The average diameter and length of sample 2 are 92.9 μm and 1200 μm. The sample stage is placed on a cold head with a constant temperature control. The stage is housed in a vacuum chamber, and the pressure inside is held below 0.5 mTorr. The measurement is conducted every 20 K at environmental temperatures from 295 K to 70 K. At lower temperatures (<70 K), denser data points (every 5–10 K) are collected to better understand low temperature (*T*) affects the electrical resistance (*R*) change.

Fig. 2(a) shows the $R \sim T$ profiles. It is very clear that when temperature changes from 295 K down to 11 K, the resistance of GMF increased by around five orders of magnitude (100,000 times). For sample 1, the resistance increases from 4387 to 3.45×10^8 Ω. And the resistance of sample 2 increases from 1422 to 8.75×10^7 Ω. This change has never been found in previous studies. More importantly, the resistances change faster and faster at low temperatures, which is totally different from graphitic film. For comparison, we also show the resistance change of a graphitic film (the width, thickness, length are 1000 μm, 1.5 nm and 1000 μm). Its resistance increases by 262% (from 5.5 kΩ to 19.9 kΩ) when temperature changes from 300 K down to 2.5 K [27]. This means the GMF fiber is extremely sensitive to temperature change, especially at low temperatures/cryogenic states. It provides a promising potential in temperature measurement. Pt is a common temperature measuring material, however, the resistance of Pt film (the width, thickness, length are 50 μm, 200 nm and 5460 μm) only decreases from 151.5 Ω to 31.2 Ω when temperature changes from 305 K down to 9.5 K. It reduces by 79.4% [28]. It should be noted that at low temperatures (<31 K), its resistance basically changes very slowly, and the sensitivity is very low. dR/dT is obtained by differentiating the *R-T* curve. The TCR value of Pt is positive while the other three materials have negative values. Fig. 2(b) shows the absolute value of TCR profiles for sample 1, sample 2 and graphitic film from RT to 10 K. The TCR value of Pt is used for comparison purpose. This relative resistance change is commonly used to evaluate the sensitivity of temperature sensors. It represents the sensitivity of the sample on how much the resistance percentage change at one degree of temperature change. The TCR value is not a constant, rather it varies with temperature and has a wide range of variation. The absolute value of TCR of the two samples are very similar. From 295 K to 230 K, it rises slowly from 0.005 K^{-1} to 0.007 K^{-1}. The value lies in a range 0.008–0.015 K^{-1} from 210 K down to 150 K. The rise accelerates staring from 130K. The range is from 0.02 K^{-1} to 0.04 K^{-1} from 130 K down to 70 K. As the temperature decreases from 60 K to 11 K, it rapidly increases from 0.05 K^{-1} to 0.5 K^{-1} by a factor of 10. Even at room temperature (RT), the sensitivity of GMF is not lower than that of graphite and Pt. The absolute value of TCR of the two GMF samples are about 0.005 K^{-1} at 295 K. For graphitic film, the absolute value of TCR is 0.0006 K^{-1} at 295 K and it increases with the decreased temperature. It is much small than that of GMF samples over the entire temperature range. The TCR of Pt is 0.002 K^{-1} at 295 K. It rises and then falls as the temperature decreases, with a maximum value at about 70K. GMF's advantage becomes higher at cryogenic temperatures. The absolute value of TCR of the two GMF samples rises rapidly with the decreased temperature and reaches 0.5 K^{-1} at 11 K. For Pt, the TCR value is less than 0.008 K^{-1}. The sensitivity of GMF is 62.5 times that of Pt. We have conducted X-ray photoelectron spectroscopy (XPS) characterization of the samples, and the results are shown in Fig. S1. The percentage of sp^2 bonding is 55.7% and the percentage of sp^3 bonding is 44.3%. We believe that the high degree of disorderness will help with thermal sensing. On one hand, the defects affect the concentration of free electrons. For carbon materials with sound structure, the resistance changes moderately when temperature changes. For example, the largest resistance change of carbon fibers is 85% from RT to 10 K [29]. High concentration of defect can severely destruct the electron transport in graphene [30]. When there are many structural defects (e.g. impurities

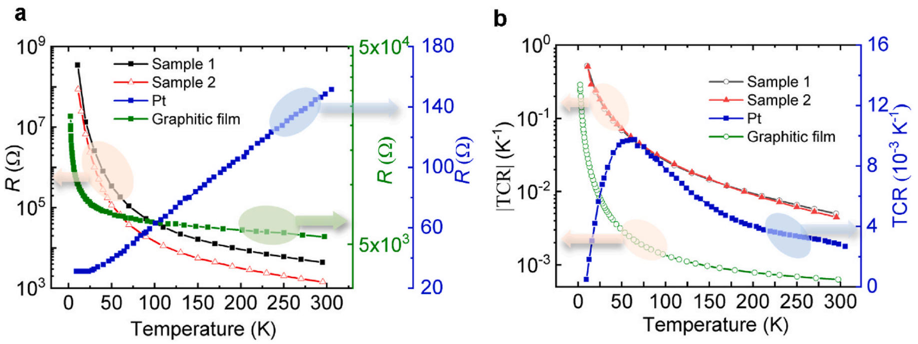

Fig. 2. (a) Temperature dependence of the electrical resistance for samples from RT to 11 K. (b) First derivative of electrical resistance against temperature divided by resistance. The literature data for Pt [28] and graphitic film [27] are plotted for comparison. (A colour version of this figure can be viewed online.)

and functional groups), the electron concentration is low, and it decreases rapidly with decreased temperature. On the other hand, the defects have a strong effect on the mean free path of free electrons. Defects may cause strong scattering of the carriers and a corresponding reduction of the conductance of graphene. The electrical conductance shows an exponential decay as the defect concentration increases [30]. Strong structural defects have great influence on electron's mean free path. The phonon-electron scattering effect becomes negligible at the presence of abundant structural defects. When temperature drops, the electron mean free path increase by phonon-freezing out is weak. Rather the quick reduction of free electron density will cause the resistance to increase quickly.

We use the following model to analyze the electrically conductive mechanism.

$$\rho^{-1}(T)=\rho_A^{-1}+\rho_B^{-1} \tag{1}$$

ρ is the temperature-independent resistivity, ρ_A is the resistivity combining the thermal activation model and the nearest-neighbor hopping (NNH) model. ρ_B is the resistivity with the variable range hopping (VRH) model.

ρ_A^{-1} can be expressed as [31].

$$\rho_A^{-1}(T)=\rho_0^{-1}\exp\left(\frac{-\Delta E_1}{k_BT}\right)+\rho_1^{-1}\exp\left(\frac{-\Delta E_2}{k_BT}\right)+\rho_2^{-1}\exp\left(\frac{-\Delta E_3}{k_BT}\right) \tag{2}$$

where k_B is the Boltzmann constant and ΔE describes the thermal activation energy of electron conduction in three temperature intervals between 295 and 60 K. Fig. S2 show $\ln\rho$ as a function of 1000/T for each temperature regime for sample 1. From these slopes, we have calculated $\Delta E_1 = 42.2$ meV, $\Delta E_2 = 31$ meV, and $\Delta E_3 = 20.2$ meV.

When temperature drops further below 60 K, the transport of electrons is analyzed using the VRH theory. The temperature dependence of GMF can be fitted by the following equation:

$$\rho_B^{-1}(T)=\rho_0^{-1}\exp\left[\left(\frac{T_0}{T}\right)^{-1/d}\right] \tag{3}$$

When $d = 4$, it can be explained by Mott VRH model. When $d = 2$, it can be explained by the Efros-Shklovskii (E-S) VRH model. Fig. S3 shows the variation of resistivity of the GMF with temperature from 60 to 11 K. The result is in good agreement with the Mott VRH's theory. Therefore, Mott VRH plays a dominant role at extremely low temperatures (60 K–11 K) for our studied samples.

4. Dynamic sensing during thermal characterization

4.1. Temperature measurement sensitivity

The extremely high sensitivity of GMF makes it an ideal material for thermal sensing. In this section, we will demonstrate this capability, investigate its temperature probing sensitivity, and also characterize its thermal transport properties, which are critical to transient response during thermal sensing. Its temperature measurement capability is assessed via dynamic sensing during transient electrical heating. When the sample is electrically heated, its temperature rises, and its own resistance change can be used to sense its temperature change. Of course, it can also be coated on other materials to observe their temperature change.

The thermal diffusivity of GMF samples at different temperatures is measured by using the transient electro-thermal (TET) technique which is an accurate and reliable method to measure the thermal diffusivity of various one-dimensional materials, such as micro-scale polyester fibers [32], single-walled carbon nanotubes bundles [32], anatase TiO_2 nanofibers [33], silkworm silks [34], graphene foam [35,36], DNA fibers [37], GFs [38], and SiC microwires [39] *etc.* The physical principle of the TET technique is based on the one-dimensional thermal transfer model. During the measurement, a step current is fed through the sample by a current source to generate transient electrical heating. This heating will increase the sample's temperature ("temperature rise" termed here). The temperature rise of the sample will result in an electrical resistance change. This temperature rise is measured by evaluating the electrical resistance change of the GMF during self-heating. Therefore it reflects the thermal sensitivity of the GMF. The temperature rise of the sample will result in an electrical resistance change. That will lead to changes in the overall voltage of the sample. Consequently, the temperature-dependent voltage gradually changes to a constant, indicating that the temperature progresses from transient to steady state. The transient voltage variation can be used to obtain the sample's effective thermal diffusivity.

The heat conduction in the GMF could be treated as one-dimensional due to the sample's high length to diameter aspect ratio. Thus, the heat transfer governing equation could be described as [40,41].

$$\frac{1}{\alpha}\frac{\partial\theta(x,t)}{\partial t}=\frac{\partial^2\theta(x,t)}{\partial x^2}+\frac{4I^2R_0}{kL\pi D^2}+\frac{4\varepsilon_r\sigma\left(T^4-T_0^4\right)}{kD} \tag{4}$$

where $\theta = T\text{-}\ T_0$, T_0 is the environment temperature, α the thermal diffusivity, k the thermal conductivity, I the constant current through the sample, and R_0 the electrical resistance before electrical heating. L and D are the length and average diameter of the sample. ε_r is the surface emissivity and σ is the Stefan-Boltzmann constant (5.67×10^{-8} W m^{-2} K^{-4}).

The normalized temperature rise (T^*) can be solved as [42]:

$$T^*\cong\frac{48}{\pi^4}\sum_{m=1}^{\infty}\frac{1-(-1)^m}{m^2}\frac{1-\exp\left[-m^2\pi^2\alpha_{eff}/L^2\right]}{m^2} \tag{5}$$

Here, α_{eff} is the effective thermal diffusivity which includes the radiation effect. The normalized temperature rise ($T^*_{\exp}$) based on the experimental data can be calculated as $T^*_{\exp} = (V_{sample} - V_0)/(V_1 - V_0)$, where V_0 and V_1 are the initial and final voltages of the sample. After obtaining $T^*_{\exp}$, we use different trial values of α_{eff} to fit the experimental results ($T^*_{\exp}$) based on Equation (2). By the least squares fitting technique, the value that gives the best fit of $T^*_{\exp}$ is taken as the effective thermal diffusivity of the sample.

The effective thermal diffusivity includes the real thermal diffusivity (α_{real}) and the radiation effect.

Therefore, α_{real} can be expressed as [32,35–37].

$$\alpha_{real}=\alpha_{eff}-\frac{1}{\rho c_p}\frac{16\varepsilon_r\sigma T_0^3}{D}\frac{L^2}{\pi^2} \tag{6}$$

At RT, the radiation effect is less than 7.4%, and it is less than 2% when temperature is below 170 K. All our experimental results have subtracted the radiation effect.

During TET experiment, the sensitive resistance/voltage change of the sample is related to the temperature sensitivity of the material. Therefore, the sensitivity can be observed through the resistance/voltage change. Fig. 3(a) is the relative resistance-time profiles for sample 1 at different temperatures: 295 K, 210 K, 110 K and 70 K. The inset is the corresponding voltage change-time profiles. It is clear the time taken to reach 90% temperature rise is 0.46 s, 0.43 s, 0.39 s and 0.3 s. This is a characteristic time usually used for thermal sensors and is the typical temperature response of our sensor. In our previous work, the temperature rise of iridium and golden film used as thermal sensor in TET experiment is around 16 K and 17.4 K at RT [43,44]. During TET measurement of graphene foam, its temperature rise is around 5 K [45]. As shown in Fig. 3(b), the temperature rise in the TET experiment using GMF for thermal sensing is less than 1 K and it decreases as the temperature goes down. This strongly demonstrates the excellent thermal sensing capability of GMF. For Sample 2, when the temperature is less than 15 K, the temperature rise is larger than 0.4 K. The reason is that the noise level is getting high as the resistance is too large. At low

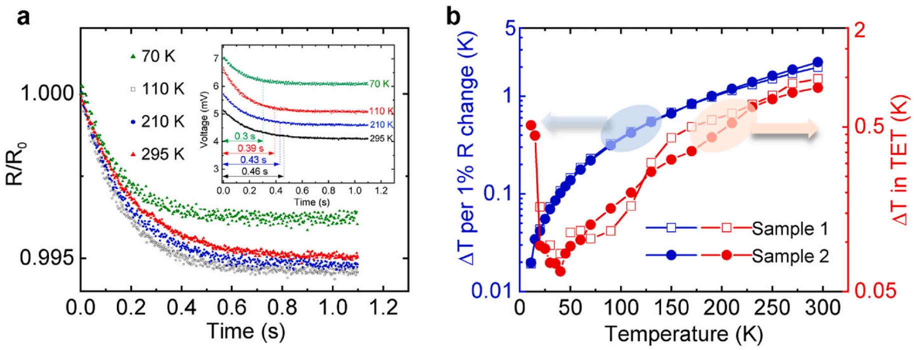

Fig. 3. (a) The relative resistance-time profiles for sample 1 at different temperatures: 295 K, 210 K，110 K and 70 K. The inset is the corresponding voltage change-time profiles. (b) The temperature rise per 1% R change and temperature rise for the two samples during TET characterization. (A colour version of this figure can be viewed online.)

temperatures (around 20 K), a temperature rise less than 0.07 K can be sensed precisely. The lowest sensible temperature rise for the two samples are 0.029 K for Sample 1 at 30 K and 0.027 K for Sample 2 at 25 K. If this GMF material is used as the sensor of TET experiment of other materials, the required temperature rise at RT can be as low as 1 K, which is much lower than the required and sensible temperature rise by using other sensing materials. If the GMF is used to measure the thermophysical properties of a material, it can achieve extremely low thermal disturbance because of the required very low temperature rise. The thermophysical properties of materials vary with temperature. At present, it is difficult to determine which temperature the measured thermophysical properties are at for TET measurement using other materials as thermal sensors. The GMF sensor makes it possible to measure the thermophysical properties of a material with a very small change in material's temperature. GMF is demonstrated to be a highly promising ultra-sensitive temperature sensor, especially at low temperatures. In Fig. 3(b), we also show how much the temperature change is at 1% resistance change since such resistance variation can be readily measured. It shows such thermal sensitivity is ~2 K at RT and 0.02 K at 10 K, which means that if there is a 1% change in resistance, then a 0.02 K temperature change can be measured, demonstrating the remarkable sensitivity of GMF sensor, especially at cryogenic state.

4.2. *Temporal response time in transient thermal probing*

The temporal response of a thermal sensor is determined by its thermophysical properties. If GMF is used for temperature measurement, it needs to be attached to the surface of the object of interest. The temperature increases when the sensor absorbs energy, and the rate of temperature increase (time response) is related to its own thermophysical properties (included ρ, c_p and k). For a suspended sensor, the characteristic thermal response time ($\Delta t_c = 0.2026L^2/\alpha$) is associated with the size of the material, here L is characteristic length. This is the time for the sensor to reach 86.7% of the final temperature rise. Such

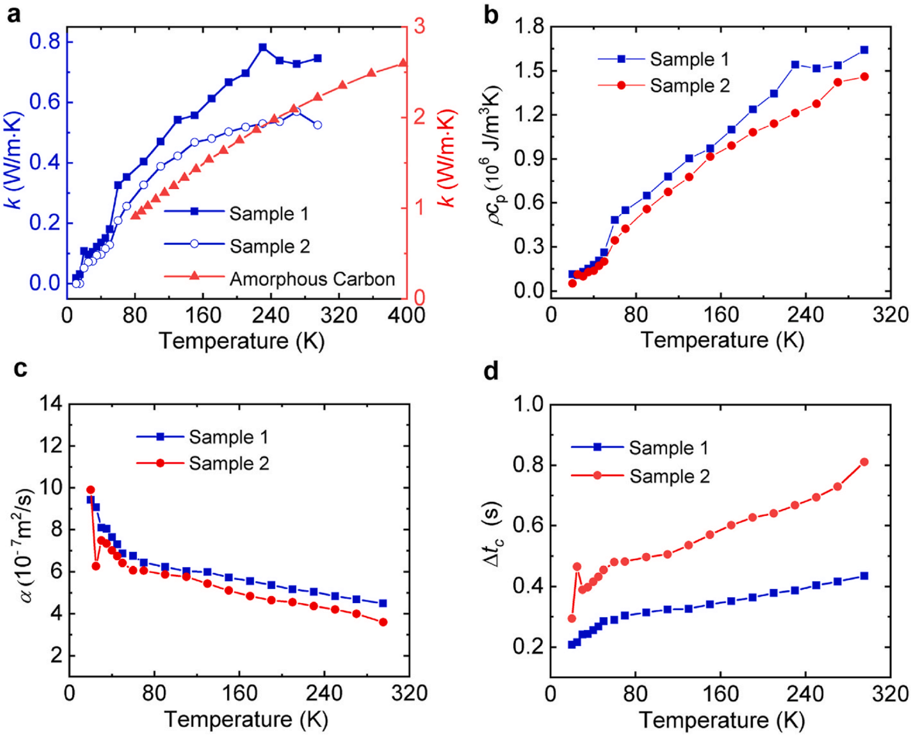

Fig. 4. (a) The measured thermal conductivity of the two GMF samples in this work. The red triangles are the literature reported k of amorphous carbon [46].(b) The volumetric specific heat of samples. (c) The measured thermal diffusivity of the two GMF samples. (d) The characteristic time in TET experiments. (A colour version of this figure can be viewed online.)

response is shown in Fig. 4(d) and is discussed in the next section.

Fig. 4(a) shows the measured thermal conductivity of the two samples. The effective thermal conductivity (k_{eff}) is obtained from $k_{eff} = I^2RL/(12A\cdot\Delta R)\cdot dR/dT$, where A is sample's cross-sectional area and ΔR is its resistance change. After subtracting the thermal radiation effect, the real k can be obtained from $k = k_{eff} - 16\varepsilon_r\sigma T^3L^2/(D\pi^2)$. As shown in the figure, the k values of both samples are very low. At RT, k is 0.75 and 0.52 W/m•K for sample 1 and sample 2, respectively. When the temperature drops, k quickly decreases and is lower than 0.18 W/m•K at temperatures below 50 K. At 20 K, the thermal conductivity of the two samples even drops to 0.11 W/m•K and 0.05 W/m•K, respectively. Such very low thermal conductivity reflects the extremely strong phonon scattering. Similarly, electrons also have strong scattering, which corresponds to the very large resistance. The material is very special, as its thermal conductivity is smaller than that of graphite and amorphous carbon. The thermal conductivity of amorphous carbon normally lies in the range 0.9–2.6 W/m•K from 400 K down to 80 K [46].

After obtaining k_{eff} and α_{eff}, the volume-based specific heat (ρc_p) of the sample can be determined as $\rho c_p = k_{eff}/\alpha_{eff}$. Fig. 4(b) shows the ρc_p for the two samples. As temperature goes down from RT to 11 K, ρc_p decreases linearly in both samples. The trend is very similar to that of graphite. As temperature drops to zero, the volume-based specific heat also goes to zero. As shown in Fig. 4 (a)–(b), the volume-based specific heat (ρc_p) and k of sample 2 are smaller than those of sample 1. It indicates that porosity is higher for sample with larger diameter. We speculate the structure is easier to shrink for smaller diameter samples during synthesis.

As shown in Fig. 4 (c), from RT to low temperatures, both α increase with temperature. α of sample 1 increases from 4.5×10^{-7}m^2/s at 295 K to 9.43×10^{-7}m^2/s at 20 K; α of sample 2 ranges from 3.6×10^{-7} m^2/s at 297 K to 9.91×10^{-7} m^2/s at 20 K. At 25 K, it has a significant drop at 6.27×10^{-7} m^2/s. When the temperature is below 20 K, the resistance of the two samples is too large and the noise level is too high to fit for thermal diffusivity. Therefore, we do not give α values below 20 K.

Fig. 4(d) is the characteristic time (Δt_c) in TET experiments. From RT down to 20 K, Δt_c of sample 1 decreases from 0.44 s down to 0.21 s, and for sample 2, Δt_c ranges from 0.81 s to 0.29 s. Both of them have very fast thermal response, which is important for temperature measurement. The length of the two sample is 983.22 and 1200 μm. If the length is shorter, for example, 100 μm, then the response speed can be further improved and will be more than 100 times faster. In comparison, the typical response time of conventional negative temperature coefficient metal oxide materials (2 mm × 2 mm × 0.2 μm) exceeds 28 s [47]. It is related to its own volume and the convection heat transfer coefficient of the surrounding medium.

In the above study, a suspended sample was used for the purpose of characterizing its thermophysical properties at the time of thermal sensing. These thermophysical properties are critical to evaluating the sensor's thermal response time in real applications. The excellent thermal sensing sensitivity of GMF is sustained by electron conduction and not by heat transfer and its related phonon scattering. So the thermal sensitivity will not be affected by substrate. We have tested it during the sample preparation stage, and did not see any substrate effect. Our current research in this direction indeed focuses on GMF that is directly attached to the surface of interest. We expect related results will be published in the near future.

5. Thermal stability and robustness of GMF

In previous sections the GMF sensor is tested at RT or cryogenic state. It could also be used at high temperatures. So, we study the properties, structure, and resistance variation by the way of annealing to investigate its robustness in thermally hostile environment. Current annealing is implemented on the sample with the same experimental setup as TET. After the sample is placed in a vacuum chamber, α_{eff} of the sample at RT is first measured using a low step current to raise the temperature as small as possible. Then a high DC current is applied to the same sample to generate large heat in the sample and complete the thermal annealing. The thermal annealing lasts for more than 120 s to ensure thermal equilibrium and accomplishment of annealing heating for one run. After the annealing treatment, we let the sample stage stay for 40 min to cool down to RT. The second α_{eff} is then measured after the sample has finished the first annealing run to investigate the effect of annealing on the electrical and thermal behaviors. The annealing run and in-situ TET measurements are then alternated by switching the form of the current between the large DC current (for annealing) and small step current (for TET measurement). The DC current increases a little at a time until the sample is burned down. This method allows an efficient monitoring of the structural changes during annealing. Errors in transferring samples between different annealing and measurement devices are successfully avoided.

The DC current of annealing for sample 1 and sample 2 are 4.8 mA and 17.2 mA, and the average temperature rise are 1062.4 K and 1097 K from our simulation results. Even after annealing the sensitivity change is not downgraded much. As shown in Fig. 5(a), before annealing it is 5 orders of magnitude variation from RT to 10 K, and it is 4.5 orders of magnitude variation after annealing, indicating that the sensibility is still very good. The resistance after annealing is smaller than that before annealing for the two samples. From RT to 10K, the resistance varies a lot, but it is very stable. For sample 1 and sample 2 before and after annealing, we measured many times, and no large instability was observed. We speculate that there are two reasons for the large resistance change with temperature. The first one is that when temperature decreases the electrons scattering mean free path decreases due to structural change, so the resistance increases. The second one is that the free electron population decreases with the decreased temperature, resulting in a rapid increase in resistance. As shown in Fig. 5, the resistance trends of the two samples are very similar. There is no thermal retention effect. In our experiment, from RT to low temperatures and back to high temperature for annealing, the whole cycle is observed normal. This very large range thermal cycle testing firmly confirms the stability of GMF as thermal sensor.

In order to better understand the improvement of the microstructure by annealing, we evaluated the thermal reffusivity (the inverse of the thermal diffusivity) of both samples to determine the effective structure domain size (l_0). The thermal reffusivity is expressed as [48,49] $\Theta = \Theta_0 + C\times e^{-\theta/2T}$ because of phonon freezing-out with decreased temperature. Obviously, as the temperature decreases, the thermal reffusivity decreases and finally reaches a constant value (Θ_0) at the 0 K limit. C is a constant and Θ_0 is known as the residual thermal reffusivity and describes the effect of defect scattering. θ is a constant that is proportional to the Debye temperature. Based on the thermal reffusivity model, the Θ_0 value and structure domain size can be extracted by fitting the thermal reffusivity ~ temperature curve. Fig. 5(b) and (d) show the temperature dependence of the thermal reffusivity before and after annealing for the two samples. The thermal reffusivity of both samples are reduced over the entire cryogenic temperature range. The fitting curves by the thermal reffusivity model are $\Theta = 1.12\times10^6 + 1.25\times10^6\times e^{(-83.6/T)}$ and $\Theta = 6.72\times10^5 + 1.15\times10^6\times e^{(-125.6/T)}$ for pre-annealed and post-annealed sample 1. The residual thermal reffusivity is determined to be 1.12×10^6 and 6.72×10^5 s/m^2. The structure domain size can be calculated as $l_0 = 3/(\Theta_0 v)$. v is phonon velocity and is estimated as 4300 m/s [50,51]. The structure domain size is determined to be 0.62 and 1.04 nm for pre-annealed and post-annealed sample 1. For sample 2, the thermal reffusivity fitting curves are $\Theta = 1.47\times10^6 + 2.71\times10^6\times e^{(-257.3/T)}$ and $\Theta = 7.75\times10^5 + 1.63\times10^6\times e^{(-151.4/T)}$, the corresponding structure domain size are 0.47 and 0.9 nm. The structure domain size increased by 68% and 91% for sample 1 and sample 2, respectively. The larger structure domain size after annealing indicates the increased grain size and fewer defects in the annealed

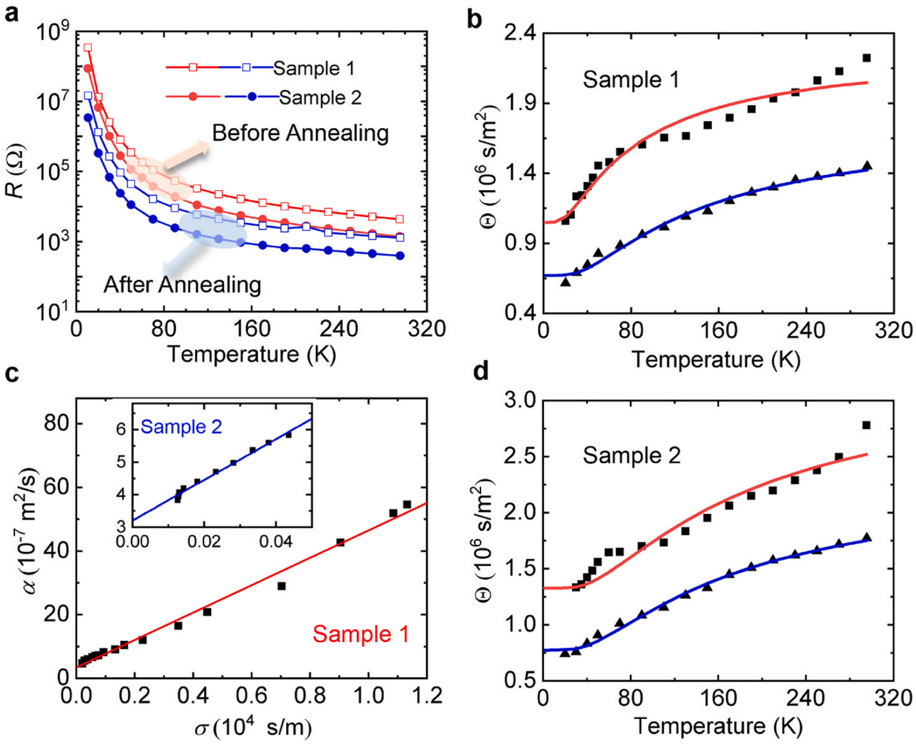

Fig. 5. (a) The resistance before and after annealing. (c) Relationship between intrinsic thermal diffusivity and electrical conductivity. (b) and (d) The temperature dependence of the thermal reffusivity before and after annealing for the two samples. (A colour version of this figure can be viewed online.)

samples.

Fig. 5(c) shows the relationship between intrinsic thermal diffusivity and electrical conductivity (σ) after different levels of annealing. The phonons and electrons in GMF both experience strong structural scattering. There is an excellent linear relation between α and σ, which is attributed to the two-component parallel structure (disordered structure and ordered structure) in GMF [52]. The relevant electrical and thermal transport direction is parallel to the internal structure alignment direction. In this way, it provides an idea for detailed structural observation because from SEM and TEM results such structure details are hard to observe.

Since the temperature distribution during annealing is not uniform, the measured thermal diffusivity and the derived thermal conductivity can be used to estimate the temperature at different locations. During annealing, since the temperatures at the two electrodes change very little during the annealing process, the k at two ends is set as the thermal conductivity of as-prepared samples. The middle point of the sample has the highest annealing temperature, leading to a maximum k at the middle point. We used 1D numerical thermal transport simulation based on the finite difference method to simulate the temperature evolution during annealing. Details of such data processing have been given in our previous work. Details of such data processing have been given in our previous work [29]. Fig. 6(a) shows the variation of sample's middle point temperature (T_m) with annealing power in the two samples. This is the highest temperature of the sample during annealing. As the annealing power increases, the temperature of the middle point reaches a certain value, under which the sample broke. The max values of T_m are determined to be 2623 and 2195 K for sample 1 and sample 2.

The resistance variations with increased annealing power for the two samples are shown in Fig. 6(b). The annealing power can be used to indicate the annealing temperature of the sample, as there is a positive correlation between annealing temperature and annealing power. At first, the resistance drops rapidly. With the increasing of annealing power, the resistance reaches quasi-saturation state and decreases slowly and eventually converges to a constant. It is due to the fact that the temperature is too high, the material becomes similar to graphite and loses its unique structure. It shows the high sensitivity, and the non-crystal nature of the structure is due to the impurities in the sample. The electrical resistance of the two samples decreased by around 98% after the final annealing. Finally, the sample breaks around the middle point as shown in Fig. 6(e). Some functional groups and gas escapes from the sample during annealing, so there are small pits in the structure. Since the temperature at the middle point is the highest during the annealing process, the fracture may be due to the structural contraction of graphene at high temperatures. Fig. 6(c) shows the variation of k_m of the middle point with annealing temperature. For the annealed samples, due to the nonuniform temperature distribution along the fiber axial direction in annealing, the whole sample is not annealed at the same level. As a result, the thermal conductivity along the fiber axial direction will be different. In our TET data processing, this non-uniform k effect is considered using numerical modeling. In the 1D numerical thermal transport simulation, the thermal conductivity along the fiber axis direction is assumed to be linearly distributed.

In general, k_m increases monotonically with annealing temperature. As temperature in the range of 300–2200 K, k_m of sample 2 increases from 0.59 to 9.18 W/m•K at a slower rate. For sample 1, k_m increases slowly from 0.75 to 6.85 W/m•K in the temperature range 337–2000 K. When the annealing temperature is above 2000 K, k_m increases faster. It increases from 6.85 to 81.67 W/m•K. We can reach a conclusion that the fiber is better annealed when the annealing temperature becomes higher, leading to greater improvement of the microstructure. Fig. 6(d) shows the variation of measured real thermal diffusivity (α_{real}) with the average temperature during the annealing process. When the average temperature increases from 500 to 1800 K, α_{real} increases by 100% and 150% for sample 1 and sample 2, respectively. The increase is attributed to the transformation of disordered structure into ordered structure, which is more pronounced at higher annealing temperatures. The annealing treatment also removes some oxygen-containing functional groups from the sp^3 carbon bonds in the atomic network of the GMF samples, which improves the internal sp^2 carbon bond structure and

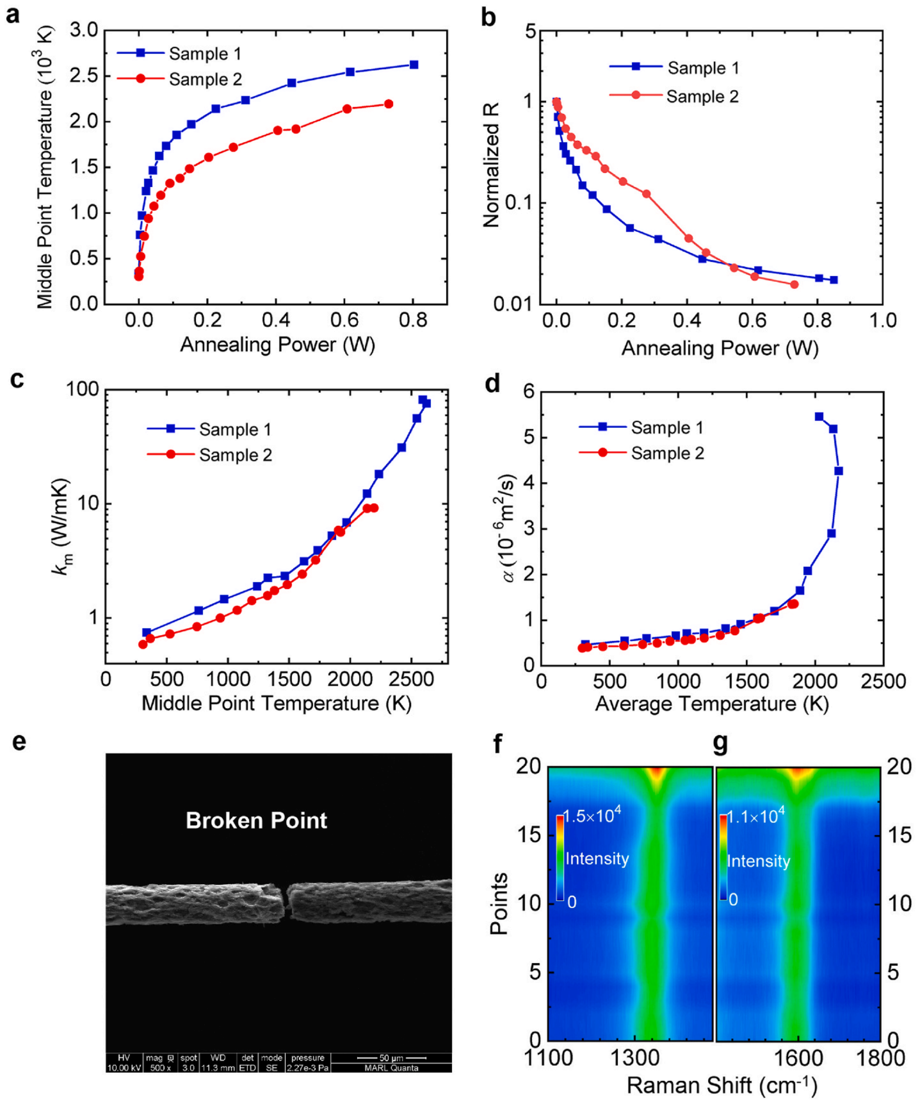

Fig. 6. (a) Temperature variations of middle point against annealing power during annealing. (b) Annealing power dependence of electrical resistance for sample 1 and sample 2. (c) Thermal conductivity of the middle point versus its annealing temperature. (d) Thermal diffusivity of the sample changes with average annealing temperature. (e) SEM image after breaking of sample 1. (f) Two-dimensional contour map to demonstrate the evolution of D peak and (g) G peak in Raman shift versus the distance from the sample end. Note all the electrical resistance, thermal conductivity and thermal diffusivity are measured after the annealing is done. (A colour version of this figure can be viewed online.)

thermal diffusivity.

Fig. 6(e) is an SEM image of the broken sample 1. More details of the sample morphologies and structure after annealing are shown in Fig. S4. After annealing, the sensing performance does not improve, but it does not downgrade much, confirming weak effect of the structure and morphology change on thermal sensing. During the annealing process, the microstructure of graphene improves and percentage of graphene increases. In addition, the functional groups in the GMFs are reduced. These two factors are responsible for the increase in electrical conductivity after annealing. Raman spectrum of sample 1 after breakdown at different locations from the broken point (Point 0) to the electrode end (Point 20) is shown in Fig. 6(f)–(g), in which the two-dimensional maps are plotted in different colors depending on the measured Raman intensity. The distance between two neighboring points is 24.6 μm. The Raman spectrum is collected under a 532 nm excitation laser. More details about the Raman measurement could be found in our previous works [53,54]. The GMF has two distinct peaks at 1350 cm^{-1} and 1580 cm^{-1}, corresponding to the D peak and G peak. After the annealing, the positions of both D and G peaks are shifted to left, suggesting that the enhanced interlayer coupling of the reduced graphene oxide [55,56].

Figure S5 shows three rounds of temperature dependence of the electrical resistance results for a GMF sample (~85 μm diameter and 2.924 mm length) attached to a glass substrate from RT to 13 K. Excellent thermal sensing capability is still observed. The sample is glued to a glass substrate with a universal adhesive since the sample cannot self-attach to the substrate during synthesis. On the other hand, the universal adhesive is a liquid when it is applied. It will penetrate into the sample, thus affecting its structure. In the actual use of GMF for temperature sensing, it is not necessary to glue the GMF to the sample to be measured. The GMF can be suspended on two small electrodes that are attached to the sample to be measured. If the GMF is used to measure temperatures of liquids and gases, it can be directly placed in gas or liquid.

Figure S6 shows three rounds of temperature dependence of the electrical resistance results of a GMF sample (1.266 mm length and 46 μm diameter) from RT to 20 K. After each cycle of experiments, we waited for two days for the next cycle of experiments. The resistance changes very little after the three wide temperature range cycles, which means the sensitivity of GMF is very robust. At RT, the resistance of round 2 changed by 3% compared with the results of round 1. The resistance of round 3 changed by 1.6% compared with the results of round 2. At 60 K, the resistance of round 2 changed by 5% compared with the results of round 1. The resistance of round 3 changed by 8% compared with the results of round 2. This resistance change is largely caused by the small structure change by the large temperature variation. It can be mitigated by structure stabilization (e.g. annealing and chemical reduction) and future work is needed in this area.

6. Conclusion

In conclusion, we reported discovery of the extreme thermal sensitivity of GMF samples synthesized by one-step dimensionally confined hydrothermal method. The resistance of GMF is extremely sensitive to temperature change, especially at low temperatures/cryogenic states. The relative resistance changing rate of the two GMF samples rose rapidly with the decrease of temperature and reached 0.5 K^{-1} at 11 K. The sensitivity of GMF is more than 62.5 times that of Pt. The thermal sensing capability of GMF sensor was fully investigated using it for dynamic measurement. A temperature rise as small as 0.027 K can be measured with high confidence at 25 K. Even after annealing the resistance change of GMF was not very large, which means the fibers still have extremely high sensitivity. This suggests excellent application and robustness of GMF thermal sensors in thermally hostile environment. For a GMF sensor of ~1 mm length, its thermal response time is around 0.2–0.8 s. This thermal response time can be reduced to the order of ms when a ~0.1 mm sample is used. GMF fibers are demonstrated to be a promising ultra-sensitive temperature sensor, especially at low temperatures.

CRediT authorship contribution statement

Huan Lin: conducted the experiment design, Formal analysis, They contributed equally to this work, conducted model development, structure characterization, data processing, Formal analysis. **Nicholas Hunter:** conducted the experiment design, Formal analysis, They contributed equally to this work, conducted model development, structure characterization, data processing, Formal analysis. **Hamidreza Zobeiri:** conducted model development, structure characterization, Formal analysis. **Yanan Yue:** conducted model development, structure characterization, Formal analysis. **Xinwei Wang:** conducted model development, structure characterization, Formal analysis, All authors worked on the manuscript preparation.

Declaration of competing interest

The authors declare the following financial interests/personal relationships which may be considered as potential competing interests: H. L. and Y. Y reports financial support was provided by National Key Research and Development Program. H.L. reports financial support was provided by Natural Science Foundation of Shandong Province. X.W. reports financial support was provided by US National Science Foundation. Y.Y. reports financial support was provided by National Natural Science Foundation of China.

Acknowledgements

This work was supported by the National Key Research and Development Program (2019YFE0119900 for H. L. and Y. Y.), the Natural Science Foundation of Shandong Province (ZR2020ME183 for H. L.), US National Science Foundation (CBET1930866 and CMMI2032464 for X. W.), and the National Natural Science Foundation of China (No. 52076156 for Y. Y.).

Appendix A. Supplementary data

Supplementary data to this article can be found online at https://doi.org/10.1016/j.carbon.2022.12.013.

References

[1] A. Feteira, Negative temperature coefficient resistance (NTCR) ceramic thermistors: an industrial perspective, J. Am. Ceram. Soc. 92 (5) (2010) 967–983.
[2] K.R. Adhikari, Thermocouple: facts and theories, Himalayan Physics 6 (2017) 10.
[3] P. Childs, J.R. Greenwood, C.A. Long, Review of temperature measurement, Rev. Sci. Instrum. 71 (8) (2000) 2959–2978.
[4] R.A. Felice, D. Nash, A, Pyrometry of materials with changing, spectrally-dependent emissivity - solid and liquid metals, AIP Conf. Proc. 1552 (1) (2013) 734–739.
[5] T. Loarer, J.J. Greffet, M. Huetz-Aubert, Noncontact surface temperature measurement by means of a modulated photothermal effect, Appl. Opt. 29 (7) (1990) 979.
[6] G.J. Edwards, Laser Emissivity Free Thermometry (LEFT), Proc of Tempmeko, 1996.
[7] A. Levick, G. Edwards, A fibre-optic based laser absorption radiation thermometry (LART) instrument for surface temperature measurement, Analytical Sciences/supplements 17 (1) (2007).
[8] E.B. Howells, Measuring temperature, Anaesth. Intensive Care Med. 19 (10) (2018) 563–567.
[9] Z. Zhen, H. Zhu, Structure and Properties of Graphene Graphene, 2018, pp. 1–12.
[10] S.M. Hollen, J.A. Gupta, Painting magnetism on a canvas of graphene, Science 352 (6284) (2016) 415–416.
[11] C. Lee, X. Wei, J.W. Kysar, J. Hone, Measurement of the elastic properties and intrinsic strength of monolayer graphene, Science 321 (5887) (2008) 385–388.
[12] K.I.B. A, K.J.S. B, Z.J.A. D, M.K. C, G.F. A, J.H. C, P.K. A, H.L.S.A.B. E, Ultrahigh electron mobility in suspended graphene, Solid State Commun. 146 (9–10) (2008) 351–355.
[13] S.V. Morozov, K.S. Novoselov, M.I. Katsnelson, F. Schedin, D.C. Elias, J. A. Jaszczak, A.K. Geim, Giant intrinsic carrier mobilities in graphene and its bilayer, Phys. Rev. Lett. 100 (2008), 016602.
[14] A.A. Balandin, S. Ghosh, W. Bao, I. Calizo, D. Teweldebrhan, F. Miao, C.N. Lau, Superior thermal conductivity of single-layer graphene, Nano Lett. 8 (3) (2008) 902.
[15] Chen Shanshan, L. Arden, Weiwei Moore, Cai, Won Ji, Suk, Raman measurements of thermal transport in suspended monolayer graphene of variable sizes in vacuum and gaseous environments, ACS Nano 5 (1) (2010) 321–328.
[16] R. Xiang, Atomic precision manufacturing of carbon nanotube —a perspective, Int. J. Extrem. Manuf. 4 (2022) 023001.
[17] A.K. Geim, Graphene: status and prospects, science 324 (5934) (2009) 1530–1534.
[18] J.H. Chen, C. Jang, S. Xiao, M. Ishigami, M.S. Fuhrer, Intrinsic and extrinsic performance limits of graphene devices on SiO2, Nat. Nanotechnol. 3 (2007) 206–209.
[19] C. Hou, H. Wang, Q. Zhang, Y. Li, M. Zhu, Highly conductive, flexible, and compressible all-graphene passive electronic skin for sensing human touch, Adv. Mater. 26 (29) (2014) 5018–5024.
[20] Q. Shao, G. Liu, D. Teweldebrhan, A.A. Balandin, High-temperature quenching of electrical resistance in graphene interconnects, Appl. Phys. Lett. 92 (20) (2008) 709, 390.
[21] U. Sassi, R. Parret, S. Nanot, M. Bruna, S. Borini, S. Milana, D. De Fazio, Z. Zhuang, E. Lidorikis, F.H.L. Koppens, Graphene-based, mid-infrared, room-temperature pyroelectric bolometers with ultrahigh temperature coefficient of resistance, Nat. Commun. (2016).
[22] J. Torres, Y. Liu, S. So, H. Yi, S. Park, J.K. Lee, S.C. Lim, M.J.A.a.m. Yun, Effects of surface modifications to single and multilayer graphene temperature coefficient of resistance, ACS Appl. Mater. Interfaces (12–43) (2020).
[23] J.J. Bae, J.H. Yoon, S. Jeong, B.H. Moon, J.T. Han, H.J. Jeong, G. Lee, H.R. Hwang, Y.H. Lee, S.Y. Jeong, Sensitive photo-thermal response of graphene oxide for mid-infrared detection, Nanoscale 7 (2015) 15695–15700.
[24] D. Kong, L.T. Le, Y. Li, J.L. Zunino, W. Lee, Temperature-dependent electrical properties of graphene inkjet-printed on flexible materials, Langmuir 28 (37) (2012) 13467–13472.
[25] Z. Dong, C. Jiang, H. Cheng, Z. Yang, G. Shi, J. Lan, L. Qu, Facile fabrication of light, flexible and multifunctional graphene fibers, Adv. Mater. 24 (14) (2012) 1856–1861.
[26] J.Y. Howe, C.J. Rawn, L.E. Jones, H. Ow, Improved crystallographic data for graphite, Powder Diffr. 18 (2) (2003) 150–154.
[27] P. Blake, P. Brimicombe, R.R. Nair, T.J. Booth, D. Jiang, F. Schedin, L. A. Ponomarenko, S.V. Morozov, H.F. Gleeson, E.W. Hill, Graphene-based liquid crystal device, Nano Lett. 8 (6) (2008) 1704–1708.
[28] J.B. Mei, J.Q. Liu, S.D. Jiang, B. Yang, C.S. Yang, Platinum resistance microsensor for cryogenic temperature measurement, Key Eng. Mater. 562–565 (2013) 198–203.
[29] J. Liu, W. Qu, Y. Xie, B. Zhu, T. Wang, X. Bai, X. Wang, Thermal conductivity and annealing effect on structure of lignin-based microscale carbon fibers, Carbon 121 (2017) 35–47.
[30] N. Liu, J. Zhao, Z. Si, Electrical conductance of graphene with point defects, ACTA PHYSICO-CHIMICA SINICA 35 (10) (2018).
[31] Y. Sun, C. Wang, L. Pan, X. Fu, P. Yin, H. Zou, Electrical conductivity of single polycrystalline-amorphous carbon nanocoils, Carbon 98 (2016) 285–290.
[32] J.Q. Guo, X.W. Wang, T. Wang, Thermal characterization of microscale conductive and nonconductive wires using transient electrothermal technique, J. Appl. Phys. 101 (6) (2007), 063537.
[33] X.H. Feng, X.P. Huang, X.W. Wang, Thermal conductivity and secondary porosity of single anatase TiO_2 nanowire, Nanotechnology 23 (18) (2012), 185701.
[34] G.Q. Liu, X.P. Huang, Y.J. Wang, Y.Q. Zhang, X.W. Wang, Thermal transport in single silkworm silks and the behavior under stretching, Soft Matter 8 (38) (2012) 9792–9799.
[35] L. Huan, X. Shen, W. Xinwei, M.J.N. Ning, Significantly reduced thermal diffusivity of free-standing two-layer graphene in graphene foam, Nanotechnology 24 (41) (2013), 415706.

[36] Y.S. Xie, Z.L. Xu, S. Xu, Z. Cheng, N. Hashemi, C. Deng, X.W. Wang, The defect level and ideal thermal conductivity of graphene uncovered by residual thermal reffusivity at the 0 K limit, Nanoscale 7 (22) (2015) 10101–10110.

[37] Z. Xu, X. Wang, H. Xie, Promoted electron transport and sustained phonon transport by DNA down to 10 K, Polymer 55 (24) (2014) 6373–6380.

[38] H. Lin, H. Dong, S. Xu, X.W. Wang, J.K. Zhang, Y.C. Wang, Thermal transport in graphene fiber fabricated by wet-spinning method, Mater. Lett. 183 (2016) 147–150.

[39] B.W. Zhu, R.D. Wang, S. Harrison, K. Williams, R. Goduguchinta, J. Schneiter, J. Pegna, E. Vaaler, X.W. Wang, Thermal conductivity of SiC microwires: effect of temperature and structural domain size uncovered by 0 K limit phonon scattering, Ceram. Int. 44 (10) (2018) 11218–11224.

[40] J. Guo, X. Wang, T. Wang, L. Zhang, Thermal characterization of micro/nanoscale one-dimensional structures using transient electro-thermal technique, J. Appl. Phys. 101 (2007), 063537.

[41] H. Lin, X. Liu, A. Kou, S. Xu, H. Dong, One-dimensional thermal characterization at the micro/nanoscale: review of the TET technique, Int. J. Thermophys. 40 (12) (2019).

[42] H. Lin, S. Xu, Y.Q. Zhang, X. Wang, Electron transport and bulk-like behavior of Wiedemann-Franz law for sub-7 nm-thin iridium films on silkworm silk, ACS Appl. Mater. Interfaces 6 (14) (2014) 11341–11347.

[43] H. Lin, S. Xu, X. Wang, N. Mei, Thermal and electrical conduction in ultra-thin metallic films: 7 nm down to sub-nm thickness, Small 9 (15) (2013) 2585–2594.

[44] Xu Shen, Yu-Qing, Ting-Ting Zhang, Xinwei Cao, Xiaoduan Wang, Tang, Thermally induced increase in energy transport capacity of silkworm silks, Biopolymers 101 (10) (2014) 1029–1037.

[45] J. Gao, D. Xie, X. Wang, X. Zhang, Y. Yue, High thermal conductivity of free-standing skeleton in graphene foam, Appl. Phys. Lett. 117 (25) (2020), 251901.

[46] A.J. Bullen, K.E. O'Hara, D.G. Cahill, O. Monteiro, A. von Keudell, Thermal conductivity of amorphous carbon thin films, J. Appl. Phys. 88 (11) (2000) 6317–6320.

[47] J. Kanungo, H. Saha, S. Basu, A.B, Chemical, Pd sensitized porous silicon hydrogen sensor-Influence of ZnO thin film, Sensor. Actuator. B Chem. 147 (1) (2010) 128–136.

[48] L. Jing, W. Qu, Y. Xie, B. Zhu, X. Wang, Thermal conductivity and annealing effect on structure of lignin-based microscale carbon fibers, Carbon 121 (2017) 35–47.

[49] H. Lin, R. Wang, H. Zobeiri, T. Wang, X. Wang, In-plane structure domain size of nm-thick MoSe 2 uncovered by low-momentum phonon scattering, Nanoscale 13 (16) (2021).

[50] C. Deng, Y. Sun, L. Pan, T. Wang, Y. Xie, J. Liu, B. Zhu, X. Wang, Thermal diffusivity of a single carbon nanocoil: uncovering the correlation with temperature and domain size, ACS Nano 10 (10) (2016) 9710–9719.

[51] G.A. Slack, Anisotropic thermal conductivity of pyrolytic graphite, Phys. Rev. 127 (3) (1962) 694–701.

[52] B. Jga, B. Hz, C. Hl, A. Dx, A. Yy, B. Xw, Coherency between thermal and electrical transport of partly reduced graphene paper, Carbon 178 (2021) 92–102.

[53] R. Wang, H. Zobeiri, H. Lin, W. Qu, X. Bai, C. Deng, X. Wang, Anisotropic thermal conductivities and structure in lignin-based microscale carbon fibers, Carbon 147 (2019) 58–69.

[54] C. Li, S. Xu, Y. Yue, B. Yang, X. Wang, Thermal characterization of carbon nanotube fiber by time-domain differential Raman, Carbon 103 (2016) 101–108.

[55] G. Wang, F. Qian, C.W. Saltikov, Y. Jiao, Y. Li, Microbial reduction of graphene oxide by Shewanella, Nano Res. 4 (6) (2011) 563–570.

[56] P. Gangwar, S. Singh, N. Khare, Study of optical properties of graphene oxide and its derivatives using spectroscopic ellipsometry, Appl. Phys. A 124 (9) (2018) 620.1–620.8.